Supplementary material for "Numerical study of the effect of surface wave on turbulence underneath. Part 2. Eulerian and Lagrangian properties of turbulence kinetic energy"

XIN GUO AND LIAN SHEN†

Department of Mechanical Engineering and St. Anthony Falls Laboratory, University of Minnesota, Minneapolis, MN 55455, USA

A. Effect of turbulence on surface wave

In this section, we discuss the effect of turbulence on the wave in terms of the Stokes drift velocity. We calculate the Stokes drift as

$$u^s = \overline{\langle u \rangle}^L. \tag{A.1}$$

The definition of the Lagrangian average $\overline{(\cdot)}^L$ is given in § 3.1 of the paper. The linear wave solution gives (Phillips 1977)

$$u^s = a^2 k \sigma \mathrm{e}^{2kz_0}. \tag{A.2}$$

Meanwhile, Phillips (2001) considered surface waves propagating over turbulent shear flow in water and derived the generalized Stokes drift as ((4.11) in his paper)

$$u^s = \frac{\partial}{\partial z} \int_0^{\kappa^*} Q_{31} \mathrm{d}\tau - \frac{1}{2} \frac{\partial^2 \overline{u}}{\partial z^2} \int_{\kappa^*}^0 \int_0^{\zeta} Q_{33} \mathrm{d}\tau \mathrm{d}\zeta. \tag{A.3}$$

Here, $\overline{(\cdot)}$ denotes the averaged value over the horizontal plane; Q_{ij} is the space–time velocity correlation expressed as

$$Q_{ij}\left(y, z, t; U\tau, 0, 0, \tau\right) = \frac{1}{L_x} \int_0^{L_x} \left(u_i\left(x, y, z, t\right) - \overline{u_i}\right) \left(u_j\left(x + U\tau, y, z, t + \tau\right) - \overline{u_j}\right) \mathrm{d}x. \tag{A.4}$$

Note that $\overline{u} = 0$ in the present study. As a result, the second term on the right hand side (RHS) of (A.3) is zero. The upper limit of the integral in the first term on the RHS of (A.3) is determined by the constraint

$$\int_0^{\kappa^* \sigma} \frac{Q_{33}}{\overline{\left(w - \overline{w}\right)^2}} \mathrm{d}\tau = 1. \tag{A.5}$$

Our DNS result and the results of (A.3) based on the wave velocity $\langle \boldsymbol{u} \rangle$ and the total velocity $\boldsymbol{u}$ are shown in figure 1. Note that the results from (A.3) are plotted up to the height of wave trough, due to the horizontal average in (A.4). Because the wave

† Email address for correspondence: shen@umn.edu.

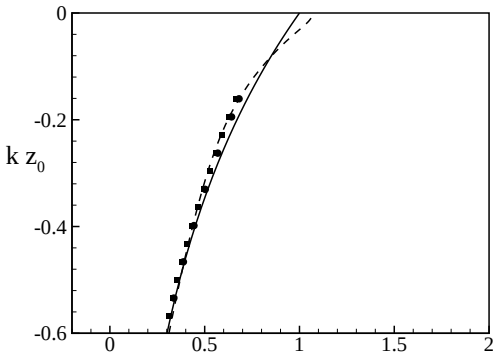

Figure 1: Vertical profiles of u^s from the present DNS (– – –), (A.2) (——), and (A.3) based on $\langle \boldsymbol{u} \rangle$ (■) and based on $\boldsymbol{u}$ (•). Results are normalized by aS. Case II_{10} is shown here.

properties of all the cases are similar (Part 1), we show the results of case II_{10} only. The difference among the four cases is manifested in turbulence, which is discussed in the result sections of the paper. As shown in figure 1, the difference among our result and the results of (A.3) based on $\langle \boldsymbol{u} \rangle$ and $\boldsymbol{u}$ is small, indicating that the effect of turbulence on the Stokes drift is small in the present study. The small turbulence effect on the wave is due to the small contribution by turbulence to the velocity correlation uw in (A.4) ($O(u'w') \sim O(0.1(u'^{rms,cf})^2) \sim O(0.001)$) compared with the contribution by wave ($O(a^2\sigma^2) \sim O(1)$). The same conclusion can also be drawn from the results shown in Part 1, where the DNS result of the wave field in the presence of turbulence agrees with the theoretical analyses and measurements of waves in literature. The comparison in figure 1 is a numerical support for the theoretical analysis of Phillips (2001). Note that if the turbulence is much stronger, e.g., turbulence intensity is more than 10 times what is considered here, the Stokes drift can be affected. The linear wave solution (A.2) is also plotted in figure 1, which is different from our DNS result in the near-surface region, due to the viscous effect of the free surface (Longuet-Higgins 1953).

B. Spectra of the normal production terms P_{xx} and P_{zz}

To further understand the energy exchange between the wave and turbulence in the wavenumber space, we study the wavenumber spectra of P_{xx} and P_{zz} (see (2.5–2.7) in the paper) defined as

$$\Psi_{P_{ii}}(k_x, z) = \frac{1}{2\pi} \int_{L_x} \overline{P_{ii}(x, y, z, t)\, P_{ii}(x + x', y, z, t)} \mathrm{e}^{-\mathrm{i}k_x x'} \mathrm{d}x' \qquad i = 1 \text{ or } 3. \quad \text{(B.1)}$$

The spectra are normalized as

$$\Psi^N_{P_{ii}}(k_x, z) = \frac{\Psi_{P_{ii}}(k_x, z)}{\left(P^{rms}_{ii}(z)\right)^2} \qquad i = 1 \text{ or } 3. \quad \text{(B.2)}$$

Figure 2(a) and (b) respectively plot $\Psi^N_{P_{xx}}$ and $\Psi^N_{P_{zz}}$ at various depths. Note that the results at $k_x > 5$ are omitted in figure 2 due to their small magnitude. Both $\Psi^N_{P_{xx}}$ and $\Psi^N_{P_{zz}}$ are the largest at $k_x = 1$, indicating that the wave and turbulence exchange energy mainly at the scale of the surface wave, consistent with the observation from figure 4 of the paper. As k_x increases, both $\Psi^N_{P_{xx}}$ and $\Psi^N_{P_{zz}}$ decrease drastically, due to the decrease

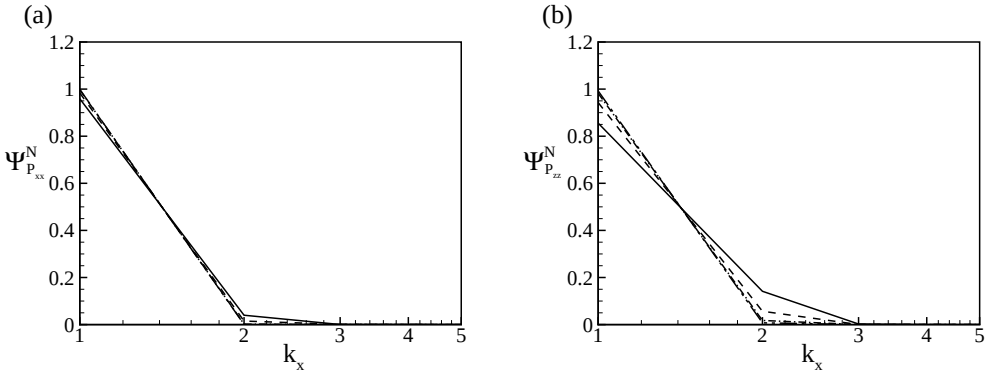

Figure 2: Normalized spectra of the normal production term (a) $\Psi^N_{P_{xx}}$ and (b) $\Psi^N_{P_{zz}}$ at $kz = -0.1$ (——), $kz = -0.2$ (– – –), $kz = -0.3$ (– · – · –), and $kz = -0.4$ (– · · – · · –). Case II_{10} is shown here.

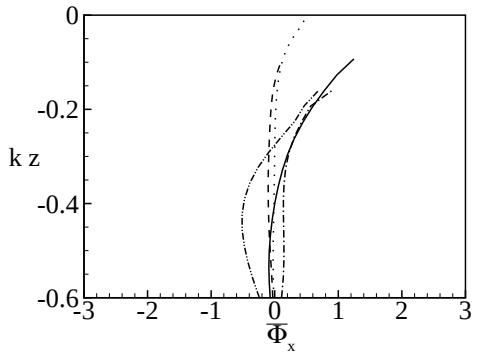

Figure 3: Vertical variation of $\overline{\Phi_x}$ for cases I_{15} (– · · – · · –), II_{10} (——), II_{15} (– · – · –), and III_{10} (– – –), and case with flat surface (· · · · · ·). The results are normalized by $2(u_i'^{rms,cf})^2/L^{cf}_{\infty}$.

of the wave strain rate at the high wavenumbers. Comparing $\Psi^N_{P_{xx}}$ with $\Psi^N_{P_{zz}}$, we find that in the near-surface region ($kz > -0.2$), $\Psi^N_{P_{zz}}(k_x = 2) > \Psi^N_{P_{xx}}(k_x = 2)$. Due to the large magnitude of u'^2 (figure 3a of the paper), $\Psi^N_{P_{xx}}$ at $k_x = 2$ is mainly due to the wave strain rate at $k_x = 2$. However, for $\Psi^N_{P_{zz}}$, due to the small magnitude of w'^2 and its relatively large variation in the near-surface region (figure 3c of the paper), $\Psi^N_{P_{zz}}$ at $k_x = 2$ is contributed not only by the wave strain rate at $k_x = 2$, but also by the correlation between $\langle w'^2 \rangle$ and $\partial\langle w \rangle/\partial z$ at $k_x = 1$. As the depth increases, the decrease of wave nonlinearity reduces the magnitude of $\Psi^N_{P_{xx}}$ and $\Psi^N_{P_{zz}}$ at $k_x \geqslant 2$.

C. Plane average of the pressure–strain correlation term Φ_x

To further understand the effect of surface wave on the blockage effect of the free surface, we plot the plane average of pressure–strain correlation term (see (2.5) in the paper), $\overline{\Phi_x}$, in figure 3. Note that the result is shown up to the height of the trough of surface wave to avoid the complexity of phase-weighted averaging. (For the region between wave crest and trough, phase-weighted formulation for Reynolds normal stress

budget should be used in a way similar to Hong & Walker 2000 and Brocchini & Peregrine 2001. The multiphase flow dynamics is however not the focus of the present study, and is thus omitted here.) As a comparison, a case with the same turbulence but a flat surface (i.e., no surface wave) is also plotted in figure 3. The $\overline{\Phi_x}$ in the flat-surface case is positive near the free surface, corresponding to the energy transfer from vertical velocity component to horizontal ones, due to the blockage effect of the surface (Perot & Moin 1995; Guo & Shen 2010). Compared with $\overline{\Phi_x}$ in the flat surface case, $\overline{\Phi_x}$ in case III_{10} is about the same, while $\overline{\Phi_x}$ in cases I_{15}, II_{10}, and II_{15} is much larger in the near-surface region, indicating that the blockage effect of the free surface is enhanced as the wave strain rate increases. Away from the free surface, Φ_i is responsible for returning turbulence to isotropy. As the depth increases, due to the combined effect of the reduction in the surface blockage effect and the anisotropy of local turbulence (§ 2.1 of the paper), $\overline{\Phi_x}$ decreases drastically. For case I_{15}, which has the strongest anisotropic turbulent motion (figure 3 of the paper), $\overline{\Phi_x}$ even becomes negative at $kz < -0.3$.

D. Decomposition of turbulence pressure

For an incompressible flow, the turbulence pressure satisfies

$$\nabla^2 p' = -2\frac{\partial \langle u_i \rangle}{\partial x_j}\frac{\partial u_j'}{\partial x_i} - \frac{\partial u_i'}{\partial x_j}\frac{\partial u_j'}{\partial x_i} + \left\langle \frac{\partial u_i'}{\partial x_j}\frac{\partial u_j'}{\partial x_i} \right\rangle, \quad p'|_{z=\eta} = p'_{fs}, \quad \left.\frac{\partial p'}{\partial z}\right|_{z=-\overline{H}} = 0. \tag{D.1}$$

Here, $\overline{H}$ is the depth of the computational domain; p'_{fs} is the turbulence pressure at the wave surface. Note that p'_{fs} should not be confused with the pressure given by the dynamic boundary condition at the free surface. The latter is of the constant value of the atmosphere pressure and is applied at the location of the instantaneous free surface. On the other hand, p'_{fs} is due to the interaction between the wave surface and turbulence. It is applied at the mean wave surface (note that η here denotes the phase-averaged surface elevation). Turbulence motion causes fluctuation in surface deformation, η', which scales with the Froude number squared, Fr^2. The resultant p'_{fs} scales with η'/Fr^2 and is thus non-zero. This result holds in the limit of $Fr \to 0$, where the free surface becomes a free-slip flat surface (see the discussion in Zhang, Shen & Yue 1999).

By decomposing the source term and the boundary condition in (D.1), we obtain

$$\nabla^2 p'^{St} = 0, \qquad p'^{St}\big|_{z=\eta} = p'_{fs}, \qquad \left.\frac{\partial p'^{St}}{\partial z}\right|_{z=-\overline{H}} = 0, \tag{D.2a}$$

$$\nabla^2 p'^{r} = -2\frac{\partial \langle u_i \rangle}{\partial x_j}\frac{\partial u_j'}{\partial x_i}, \qquad p'^{r}|_{z=\eta} = 0, \qquad \left.\frac{\partial p'^{r}}{\partial z}\right|_{z=-\overline{H}} = 0, \tag{D.2b}$$

$$\nabla^2 p'^{s} = -\frac{\partial u_i'}{\partial x_j}\frac{\partial u_j'}{\partial x_i} + \left\langle \frac{\partial u_i'}{\partial x_j}\frac{\partial u_j'}{\partial x_i} \right\rangle, \qquad p'^{s}|_{z=\eta} = 0, \qquad \left.\frac{\partial p'^{s}}{\partial z}\right|_{z=-\overline{H}} = 0. \tag{D.2c}$$

Here, the superscripts 'St', 'r', and 's' denote the Stokes, rapid, and slow components, respectively.

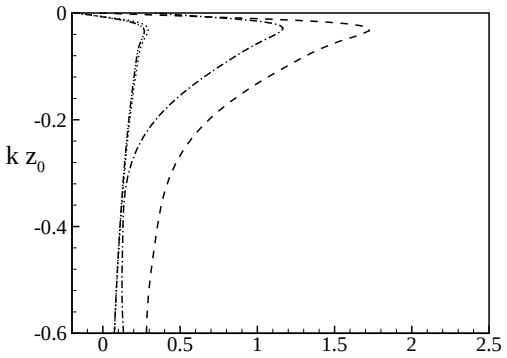

Figure 4: Vertical profiles of – · – · –, $\overline{\partial\langle u\rangle/\partial z}^{L}$, · · · · · ·, $\mathcal{U}_{xz}$, – · · – · · –, $\mathcal{U}_{zz}$, and – – –, $\mathrm{d}u^s/\mathrm{d}z_0$ from the present DNS. Results are normalized by $2akS$. Case II_{10} is shown here.

E. Difference between $\mathrm{d}u^s/\mathrm{d}z_0$ and $\overline{\partial\langle u\rangle/\partial z}^{L}$

Using (A.1), (3.1) of the paper, and the chain rule, we rewrite $\mathrm{d}u^s/\mathrm{d}z_0$ as

$$\frac{\mathrm{d}u^s}{\mathrm{d}z_0} = \frac{\mathrm{d}}{\mathrm{d}z_0}\left(\frac{1}{T_L}\int_{t_0}^{t_0+T_L} u^{\mathbf{\Pi}}\mathrm{d}t\right) = \underbrace{\frac{1}{T_L}\int_{t_0}^{t_0+T_L}\left(\frac{\partial\langle u\rangle}{\partial x}\right)^{\mathbf{\Pi}}\frac{\partial\Pi_x}{\partial z_0}\mathrm{d}t}_{\mathcal{U}_{xz}} + \underbrace{\frac{1}{T_L}\int_{t_0}^{t_0+T_L}\left(\frac{\partial\langle u\rangle}{\partial z}\right)^{\mathbf{\Pi}}\mathrm{d}t}_{\overline{\frac{\partial\langle u\rangle}{\partial z}}^{L}}$$
$$+ \underbrace{\frac{1}{T_L}\int_{t_0}^{t_0+T_L}\left(\frac{\partial\langle u\rangle}{\partial z}\right)^{\mathbf{\Pi}}\frac{\partial\Pi_z}{\partial z_0}\mathrm{d}t}_{\mathcal{U}_{zz}}. \qquad \text{(E.1)}$$

As (E.1) shows, $\mathrm{d}u^s/\mathrm{d}z_0$ is related to $\overline{\partial\langle u\rangle/\partial z}^{L}$ as well as $\mathcal{U}_{xz}$ and $\mathcal{U}_{zz}$, where $\mathcal{U}_{xz}$ represents the correlation between $(\partial\langle u\rangle/\partial x)^{\mathbf{\Pi}}$ and $\partial\Pi_x/\partial z_0$, and $\mathcal{U}_{zz}$ represents the correlation between $(\partial\langle u\rangle/\partial z)^{\mathbf{\Pi}}$ and $\partial\Pi_z/\partial z_0$.

We plot in figure 4 the vertical profiles of $\overline{\partial\langle u\rangle/\partial z}^{L}$ (which has been studied in Part 1 and is shown here for comparison), $\mathcal{U}_{xz}$, $\mathcal{U}_{zz}$, and $\mathrm{d}u^s/\mathrm{d}z_0$. Due to the similar wave properties among the four simulation cases (Part 1), only the result of case II_{10} is shown here. In the deep region, $\overline{\partial\langle u\rangle/\partial z}^{L}$, $\mathcal{U}_{xz}$, and $\mathcal{U}_{zz}$ make comparable contributions to $\mathrm{d}u^s/\mathrm{d}z_0$. As the free surface is approached, although both $\mathcal{U}_{xz}$ and $\mathcal{U}_{zz}$ increase to their maxima near the free surface, their relative contributions to $\mathrm{d}u^s/\mathrm{d}z_0$ are relatively small compared with $\overline{\partial\langle u\rangle/\partial z}^{L}$ due to the large value of the latter there. Nevertheless, figure 4 shows that $\mathcal{U}_{xz}$ and $\mathcal{U}_{zz}$ make noticeable difference between $\mathrm{d}u^s/\mathrm{d}z_0$ and $\overline{\partial\langle u\rangle/\partial z}^{L}$.

F. Vertical profiles of P_{13}^{LL}, P_{13}^{ll}, and P_{31}^{LL}

Figure 5 shows the vertical profiles of P_{13}^{LL}, P_{13}^{ll}, and P_{31}^{LL} (see § 3 of the paper) of case II_{10}. The P_{13}^{LL} and P_{31}^{LL} are close to zero at the free surface due to the small value of $\overline{\langle u'w'\rangle}^{L}$, of which the vertical profiles are shown in figure 6. As the depth increases, P_{13}^{LL} increases to its maximum at around $kz_0 = -0.1$ and then decreases gradually to about

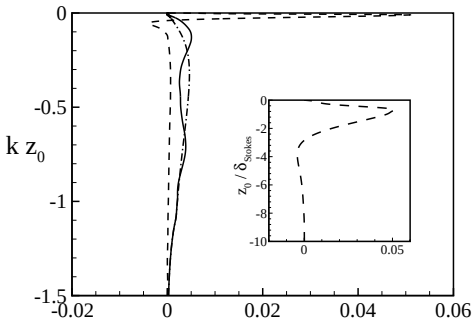

Figure 5: Vertical profiles of dominant components in shear production: ——, P_{13}^{LL}, – – –, P_{13}^{ll}, and – · – · –, P_{31}^{LL}. The inset shows a zoom view of P_{13}^{ll} in the near-surface region. The results are normalized by $2(u_i'^{rms,cf})^2 S$. Case II_{10} is shown here.

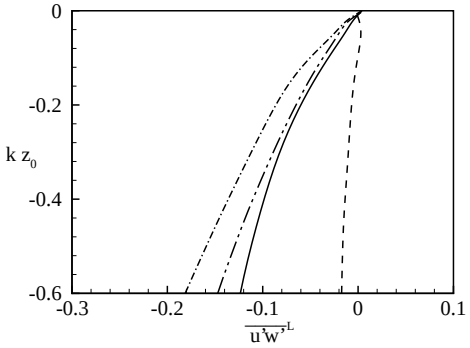

Figure 6: Vertical profiles of $\overline{u'w'}^L$ for cases I_{15} (– · – · –), II_{10} (——), II_{15} (– · – – · – –), and III_{10} (– – –). The result is normalized by $(u'^{rms,cf})^2$.

zero in the deep region. The increase is due to the increase of both $\overline{\langle u'w'\rangle}^L$ (figure 6) and $\overline{\partial\langle u\rangle/\partial z}^L$ (figure 4; also discussed in Part 1) near the free surface. The decrease of P_{13}^{LL} in the deep region is mainly due to the decrease of $\overline{\partial\langle u\rangle/\partial z}^L$. As the depth increases, compared with P_{13}^{LL}, P_{31}^{LL} reaches its maximum at a deeper location around $kz_0 = -0.3$. This difference is because $\overline{\partial\langle w\rangle/\partial x}^L$ decreases uniformly from the free surface to the deep region, whereas $\overline{\partial\langle u\rangle/\partial z}^L$ first increases from a small value at the free surface to its maximum and then decreases towards the deep region. Thus, the increase of P_{31}^{LL} is contributed only by the increase of $\overline{\langle u'w'\rangle}^L$ near the free surface. The decrease of P_{31}^{LL} is due to the decrease of $\partial\langle w\rangle/\partial x$ in the deep region.

Next, we discuss P_{13}^{ll}. As shown in the inset of figure 5, as the depth increases, P_{13}^{ll} increases from a small value at the free surface, reaches its maximum near the free surface, decreases drastically to a small negative value, and then approaches zero in the deep region. This variation is consistent with the distribution of θ_{13} discussed in Appendix B of the paper. The small value of P_{13}^{ll} at the free surface and in the deep region is caused by the θ_{13} values near $3\pi/2$ and $\pi/2$ in these two regions, respectively (see figure 6 and (B3) of the paper). The P_{13}^{ll} reaches its maximum at a short distance below the free

surface where $\theta_{13} \approx \pi$. Therefore, P_{13}^{ll} is associated with the viscous effect of the free surface and contributes to the net energy transfer from the wave to turbulence mainly in the near-surface region.

REFERENCES

Brocchini, M. & Peregrine, D. H. 2001 The dynamics of strong turbulence at free surfaces. Part 2. Free-surface boundary conditions. *J. Fluid Mech.* **449**, 255–290.

Guo, X. & Shen, L. 2010 Interaction of a deformable free surface with statistically-steady homogeneous turbulence. *J. Fluid Mech.* **658**, 33–62.

Hong, W.-L. & Walker, D. T. 2000 Reynolds-averaged equations for free-surface flows with application to high-Froude-number jet spreading. *J. Fluid Mech.* **417**, 183–209.

Longuet-Higgins, M. S. 1953 Mass transport in water waves. *Phil. Trans. A* **245**, 535–581.

Perot, B. & Moin, P. 1995 Shear-free turbulent boundary layers. Part 1. Phyiscal insights into near-wall turbulence. *J. Fluid Mech.* **295**, 199–227.

Phillips, O. M. 1977 *Dynamics of the Upper Ocean*. Cambridge University Press.

Phillips, W. R. C. 2001 On the pseudomomentum and generalized Stokes drift in a spectrum of rotational waves. *J. Fluid Mech.* **430**, 209–229.

Zhang, C., Shen, L. & Yue, D. K. P. 1999 The mechanism of vortex connection at a free surface. *J. Fluid Mech.* **384**, 207–241.